Diffuse optical imaging using spatially and temporally modulated light

Thomas D. O'Sullivan
Albert E. Cerussi
David J. Cuccia
Bruce J. Tromberg

Diffuse optical imaging using spatially and temporally modulated light

Thomas D. O'Sullivan,[a] **Albert E. Cerussi,**[a] **David J. Cuccia,**[b] **and Bruce J. Tromberg**[a]
[a]University of California, Irvine, Laser Microbeam and Medical Program (LAMMP), Beckman Laser Institute and Medical Clinic, Irvine, California
[b]Modulated Imaging Inc., Irvine, California

Abstract. The authors describe the development of diffuse optical imaging (DOI) technologies, specifically the use of spatial and temporal modulation to control near infrared light propagation in thick tissues. We present theory and methods of DOI focusing on model-based techniques for quantitative, *in vivo* measurements of endogenous tissue absorption and scattering properties. We specifically emphasize the common conceptual framework of the scalar photon density wave for both temporal and spatial frequency-domain approaches. After presenting the history, theoretical foundation, and instrumentation related to these methods, we provide a brief review of clinical and preclinical applications from our research as well as our outlook on the future of DOI technology. © *2012 Society of Photo-Optical Instrumentation Engineers (SPIE).* [DOI: 10.1117/1.JBO.17.7.071311]

1 Introduction

1.1 Background

Optical imaging is a powerful approach for visualizing tissue structure and function across spatial scales ranging from micrometers to centimeters. Tissue optical imaging technologies are generally discussed in two broad regimes, microscopic and macroscopic, which are based on controlling and measuring coherent and diffuse light-tissue interactions, respectively. This tutorial describes the development of diffuse optical imaging (DOI) and the use of spatial and temporal modulation techniques to control light propagation with the intent to quantitatively measure tissue absorption and scattering properties.

DOI typically relies on red and near-infrared (NIR) light ($\sim$600 to 1000 nm) to probe optical properties in centimeter-thick living tissues. At distances greater than 1 to 2 mm from a source, photons can be modeled as particles that behave according to Fick's first law of diffusion (typically used to describe bulk transport of molecules or heat), traveling randomly through the tissue.[1] This approximation is valid because NIR light scattering occurs much more frequently than absorption. Multiply scattered photons carry information about spatially averaged absorption and scattering properties along the propagation path. The typical mean free path to an NIR absorption event in tissue is $\sim$10 cm, while scattering lengths are $\sim$20 to 40 μm. Thus, even though light may enter the tissue in a small spot from a collimated, coherent laser source, after $\sim$1 mm of propagation, the light is largely incoherent and nearly isotropic, spread out over an expanded volume. This results in image performance that is influenced by the transport scattering length, $l_{\text{tr}} = 1/(\mu_a + \mu_s') \sim$1 mm, where μ_a and μ_s' are the tissue absorption (μ_a) and reduced scattering (μ_s') coefficients. Consequently, DOI resolution and depth can range from $\sim l_{tr}$ to $\sim$100l_{tr}, respectively, depending on the precise imaging geometry and characteristics of the light source.

The organization of tissue structural elements, primarily cells and extracellular matrix proteins, influences spatial variations in tissue refractive index and bulk scattering properties. DOI is sensitive to these anatomic features as well as the presence of light absorbing and emitting molecules. DOI molecular contrast is derived from exogenous contrast agents, such as administered fluorescent molecules and genetically induced luminescent proteins, as well as endogenous molecules (chromophores) that absorb red-NIR light, such as oxygenated (O_2Hb) and reduced (deoxygenated) hemoglobin (HHb), water, lipids, porphyrins, and cytochromes. One of the goals of DOI is to quantify absorption, fluorescence, and scattering contrast in thick tissues. Unlike conventional anatomic imaging methods (e.g., x-ray, ultrasound, and MRI), DOI is mainly a low resolution functional imaging method that is most sensitive to biological and physiological processes, such as tissue perfusion and metabolism.

1.2 Diffuse Imaging Approaches

Several different DOI approaches are used to characterize tissue optical properties, including time-independent [also known as continuous wave (CW), or DC] and time-dependent (i.e., AC) methods. Both AC and DC methods can be performed in real or frequency domains, with the goal of interrogating tissues on sufficiently different spatial and/or temporal scales in order to resolve scattering from absorption using model-based analyses. Thus, methods that resolve these events in space and/or time, in conjunction with transport model-based analyses, can be used to independently recover tissue optical absorption and scattering properties. This is possible due to the fact that mean length- and time-scales for scattering and absorption are, respectively,

on the order of $l_{sc} \sim 20$ to $40 ~\mu m$, $\tau_{sc} \sim 0.1$ ps; and $l_{abs} \sim$ 10 cm, $\tau_{abs} \sim 0.2$ ns.

Many CW techniques in widespread use are not transport model-based. They measure the reflectance or transmittance of a sample without regard to the individual contributions of absorption and scattering separately. CW instrumentation is fast, inexpensive, commercially accessible, and is useful for measuring relative changes in tissue chromophores. When multiple wavelengths are used, this is commonly referred to as NIR spectroscopy (NIRS). Typical clinical instruments are dedicated to measuring percent tissue oxygenation, $\%StO_2$, which is the fraction of total tissue hemoglobin that is oxygenated [i.e., $100 \times (O_2Hb/total\,Hb)$]. CW-NIRS measurements generally do not consider tissue scattering changes and are primarily used in brain and muscle in order to longitudinally monitor hemodynamics in an individual patient.[2]

Time-domain (or time-resolved) techniques, in contrast, deliver pulses of light (typically a few picoseconds) to the tissue and use time-gated and/or single photon counting detectors to measure the attenuation and broadening of the source pulse after propagation through the tissue.[3] An analysis of the detected pulse (e.g., the temporal point-spread function—t-PSF) can accurately distinguish between tissue absorption and scattering properties. For example, photons arriving at the tail of the detected pulse are delayed by many more scattering events, and thus have had a greater probability of being influenced by the low density of NIR tissue absorbers.

Temporal frequency-domain photon migration (FDPM) also separates absorption and scattering properties, but instead of using pulsed light, FDPM involves launching light into the tissue that is intensity modulated at hundreds of MHz. At these modulation frequencies, multiple scattering causes the incident scalar wave of fluctuating photon density to effectively slow down. This reduced photon density wave (PDW) phase velocity is manifested as a phase shift between the detected and source signals. Absorption and scattering information is apparent in both the PDW amplitude attenuation and the phase shift. By applying the proper physical model of photon migration (to be discussed below), the measured relative phase and amplitude together provide an accurate estimation of optical properties. FDPM can be performed at single or multiple modulation frequencies. Sweeping through many modulation frequencies yields the Fourier transform equivalent of a portion of the time domain temporal modulation transfer function (t-MTF).

Spatial frequency-domain imaging (SFDI) is the spatial analog to FDPM, except instead of modulating the light source in time, it is modulated in space. Patterns of light (e.g., stripes of light and dark) are projected onto the tissue at different spatial frequencies and phases, and the resulting reflectance is measured with an imaging camera. Tissue serves as a low-pass filter causing the high frequency components (closely spaced stripes) to be blurred. Thus lower spatial frequency patterns are primarily sensitive to absorption, while scattering strongly dominates high frequency reflectance. SFDI is advantageous compared to other DOI techniques in that it provides non-contact wide-field imaging of tissue absorption and scattering properties. In contrast to methods that rely on contact fibers and probe centimeter depths, SFDI is commonly used in a planar reflectance geometry, which limits sensitivity to depths of ~5 mm.

We emphasize that whether the measurement technique utilizes a time-dependent signal (time-domain and FDPM), or a time-independent signal (CW and SFDI), DOI methods are related via the Fourier transform (see Fig. 1). For the time-varying methods, the Fourier transform of the pulse in the "real" time domain is equivalent to a temporally broadband frequency domain sweep. This equivalency extends to the spatial domain, in which a measurement of the spatial point spread function (s-PSF) is related to the spatial modulation transfer function (s-MTF).

1.3 Scope of This Work

In this tutorial we present the theory and methods of DOI focusing on techniques that quantitatively measure endogenous absorption and scattering contrast in human subjects. We specifically emphasize the common conceptual framework of the scalar PDW for both temporal and spatial frequency-domain approaches. After presenting the history, theoretical foundation, and instrumentation, we provide a review of applications using these methods taken primarily from our research. The techniques presented here are the building-blocks of diffuse optical tomography (DOT), which employs many source-detector pairs to reconstruct 3-dimensional images of optical properties. DOT will not be discussed in this tutorial, but there are several excellent reviews on DOT methods and applications.[5–8]

2 Theory of Diffuse Optics

2.1 Light Propagation in Thick Tissue

Light propagation in any material can be described by Maxwell's equations; however, dense scattering in turbid media creates a complex superposition of waves and boundary conditions that cannot easily be solved analytically (or numerically by today's computing power). As a result, we refer to the transport theory of photons, which treats light as noninteracting particles.[9,10] The radiative transfer equation (RTE, or Boltzmann equation) is an approximation to Maxwell's equations, based upon conservation of energy, describing the propagation of photons and energy through space and time. While it is difficult to solve the full expression analytically and numerically,[11] assumptions made to the RTE applicable to photon movement in tissue result in simpler analytical solutions. The most commonly used is the P_l approximation, which keeps the first-order term of a spherical expansion of the RTE (called the P_n approximation). Excellent reviews on this topic exist.[12,13]

For an isotropic point source inside a homogeneous medium, the P_l approximation expresses the photon density, $U(\mathbf{r}, \omega)$, as a function of the optical properties:[14–16]
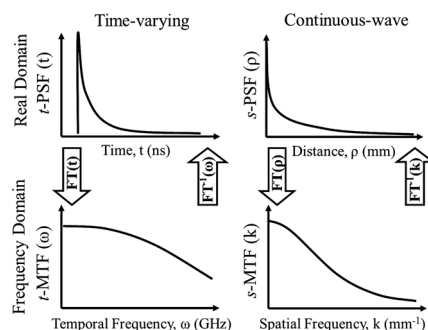
Fig. 1 Four measurement domains of DOI: time domain (top left), temporal frequency domain (bottom left), real spatial domain (top right), and spatial frequency domain (bottom right). Figure reproduced with permission from Ref. 4.

$$[\nabla^2 - k^2(\omega)]U(\mathbf{r}, \omega) = -\frac{S(\omega)}{vD}\exp[-i\phi_0(\omega)]\delta(\mathbf{r}) \qquad (1)$$

$$k^2(\omega) = \frac{\mu_a}{D}\left[1 - i\frac{\omega}{v\mu_a}(1 + 3\mu_a D)\right], \qquad (2)$$

where ω is the temporal modulation frequency. This relationship is written in the temporal frequency domain [e.g., $U(r, t) = U(r, \omega)\exp(-i\omega t)$, etc.], where v is the speed of light inside the medium, $S(\omega)\exp[-i\phi_0(\omega)]\delta(\mathbf{r})$ is a point source with a frequency-dependent amplitude and phase, centered at $r = 0$, and $D = (3\mu_s' + 3\mu_a)^{-1}$ is the optical diffusion coefficient. The variables $|\mathbf{r}|$ and t represent distance from the source and time, respectively. μ_a is the absorption coefficient $\mu_s' = (1 - g)\mu_s$ and is the reduced scattering coefficient. These are the wavelength-dependent quantities to be measured by DOI. The reduced scattering takes into account both the probability of encountering a scattering event as well as the direction the photon is likely to take as a result of the event. g is the average cosine of the scattering angle. The spherical harmonics expansion is valid under the assumptions that 1. the medium is macroscopically homogeneous, 2. the described region is far from sources and boundaries (i.e., more than one transport mean free path), and 3. the medium is strongly scattering (i.e., $\mu_s \gg \mu_a$).

To solve this equation for photon density, we need to apply boundary conditions. For simplicity, we first assume that the medium is infinite, $U(r, \omega) \to 0$ as $r \to \infty$, and we find a one-dimensional solution to Eq. (1):

$$U(r, \omega) = \frac{S(\omega)\exp[-i\phi_0(\omega)]}{4\pi vD}\frac{1}{r}\exp[-k(\omega)r]. \qquad (3)$$

The frequency-domain solution is a damped spherical wave, or in this case, a diffusely propagating PDW with a wave vector, k, that is a function of the temporal modulation frequency, ω, and the tissue optical properties. The phase $\Theta_{\text{inf}}(r, \omega)$ and amplitude $A_{\text{inf}}(r, \omega)$ of the PDW are:

$$\Theta_{\text{inf}}(r, \omega) = k_{\text{imag}}(\omega)r + \phi_0$$
$$A_{\text{inf}}(r, \omega) = \frac{S(\omega)}{4\pi Dr}\exp[-k_{\text{real}}(\omega)r]. \qquad (4)$$

Equation (3) gives us a solution that describes the light distribution that results from an isotropic point source placed inside an infinite medium. In tissue imaging, we commonly introduce the light externally, such as from the skin surface, so we need to apply this important boundary condition. In this case, after light enters the tissue, it can undergo Fresnel reflections at the tissue-air interface due to the refractive index mismatch. If the boundary is not accounted for, optical property reconstruction can be in error of 50% or more.[16] There are two common approaches taken to apply this semi-infinite boundary condition, the partial-current and extrapolated boundary methods.[17] The extrapolated boundary method, for example, corrects for the additional reflection at the interface by introducing a virtual source placed somewhere above the boundary.

2.2 Measuring Chromophore Concentration

Once the absorption coefficient of a volume of tissue is known at two or more wavelengths, it is possible to estimate the absolute concentration of chromophores present in that volume by applying the Beer-Lambert law. Assuming that the measured absorption coefficients represent a linear combination of the chromophore spectra (i.e., individual chromophore absorption is independent), we can solve a system of linear equations to estimate absolute quantities. The following matrix equation relates the wavelength-dependent absorption coefficient as a function of the molar extinction spectra (ε), and tissue chromophore concentration (C):

$$\vec{\mu}_a(\lambda) = 2.303[\varepsilon(\lambda)]\vec{C}. \qquad (5)$$

At a minimum, to solve for n tissue chromophore components, absorption coefficients must be known at n different wavelengths where the chromophores exhibit nonnegligible absorption. Greater accuracy is obtained by sampling at more wavelengths and solving the overdetermined system (e.g., with least squares fitting). The only constraint that is routinely employed is that concentrations must have positive values; no other *a priori* knowledge is required.

Since hemoglobin is a relatively strong NIR absorber with distinct features, only two wavelengths are necessary in the $\sim$650 to 900 nm region to estimate the tissue concentration (μM) of ctO_2Hb and $ctHHb$ using published hemoglobin extinction coefficients.[18] With that information, one also knows total tissue hemoglobin ($ctTHb = ctO_2Hb + ctHHb$) and % oxygen saturation ($stO_2 = 100 \times ctO_2Hb/ctTHb$). With additional wavelengths (e.g., greater than 900 nm), it is possible to estimate percent water (ctH_2O) and bulk lipid ($ctLipid$) which have absorption peaks in the $\sim$960 and $\sim$920 nm regions, respectively. Pure water and lipid spectra at 100% concentration are used, which corresponds to 55.6 M and 0.9 g ml^{-1}, respectively.[19,20] Water extinction coefficients have been obtained by measuring distilled water in a cuvette using a spectrophotometer (Beckman DU 650) at various temperatures in order to account for possible temperature effects. Lipid extinction coefficient values have been obtained from mammalian fat spectra.[21]

3 Frequency Domain Photon Migration

In temporal frequency-domain measurements, intensity-modulated laser light creates PDWs that propagate through the tissue.[22] A photodetector samples the light some distance away from the source after interacting with the tissue, and the oscillating signal is compared to the source light to measure relative changes in amplitude and phase [Fig. 2(a)]. Light can be detected in either reflection or transmission geometry through a section of thick tissue. At the detector, placed a distance r away from the source, photon density is diminished in amplitude and delayed in phase [Fig. 2(b)], but remains at the same modulation frequency.

While Eqs. (1)–(5) (and the solutions relevant to the semi-infinite boundary condition) describe the source distribution and are useful for analyzing how much light is delivered to the tissue, to calculate optical properties, we are most interested in modeling the detectable light after it exits the tissue. Using the method of images to correct for the semi-finite medium, the equation describing phase and amplitude of the detected PDW at a detector a distance from the source is given by:

$$\Theta_{\text{inf}}(\rho, \omega) = k_{\text{imag}}(\omega)r_a - \arctan\left(\frac{\eta}{\xi}\right) + \phi_0(\omega) \qquad (6)$$
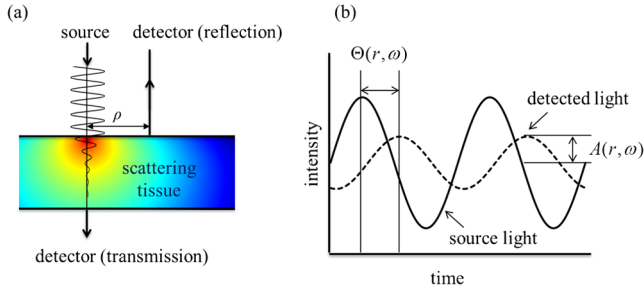
Fig. 2 Measurement of optical properties with FDPM; (a) A temporally modulated light source creates PDWs, which are attenuated in the tissue. The attenuated light can be detected in either reflection or transmission geometries. (b) The detected signal is diminished in amplitude and delayed in phase with respect to the source.

$$A_{\text{si}}(\rho, \omega) = \frac{S(\omega)}{4\pi v D} \sqrt{\xi^2 + \eta^2}, \qquad (7)$$

where

$$\xi = \frac{1}{r_a} \exp[-k_{\text{real}}(\omega) r_a] - \cos[k_{\text{imag}}(\omega)(r_t - r_a)]$$

$$\times \frac{1}{r_t} \exp[-k_{\text{real}}(\omega) r_t]$$

$$\eta = \sin[k_{\text{imag}}(\omega)(r_t - r_a)] \frac{1}{r_t} \exp[-k_{\text{real}}(\omega) r_t] \qquad (8)$$

and

$$r_a = \sqrt{\rho^2 + (l_{\text{tr}})^2} \qquad r_t = \sqrt{\rho^2 + (2z_b l_{\text{tr}})^2}. \qquad (9)$$

where $z_b = \frac{2}{3} \frac{1 + R_{eff}}{1 - R_{eff}} l_{tr}$ is the location of extrapolated boundary, where R_{eff} represents an effective Fresnel coefficient for the tissue-outside medium interface. Haskell et al. have calculated this coefficient to be 0.493 and 0.431 when the air tissue interfaces are $n = 1.4$ and 1.3, respectively,[16] leading to z_b approximately being equal to 2 mm. Here we have presented the parameters phase and amplitude, which are directly measured by FDPM instrumentation. These measurements, taken at some distance r from a modulated source, are fit to the model of photon migration to estimate $\mu_a(\lambda)$ and $\mu'_s(\lambda)$

Applying frequency-domain methods to measuring optical properties was a logical extension of the time-domain techniques that were being explored in the late 1980s.[23–25] In the early 1990s, several groups reported the application of FDPM for the measurement of optical properties in tissue-simulating phantoms and/or live tissue.[26–30] Very rapidly, important breakthroughs in both modeling and technology followed. This included the important observation by Gratton and colleagues that PDWs behave like scalar density waves,[27] displaying properties of interference,[31] refraction,[32] scattering,[33] diffraction,[17] and dispersion.[22,34] Technology advances in RF electronics, driven by the telecommunications industry, enabled the miniaturization and compact integration of components required for FDPM measurements. FDPM techniques have since been applied in brain, muscle, and breast imaging, and there are commercial devices available.[2]

In order to enhance the spectral bandwidth of FDPM, our group has combined the principles of CW-NIRS and FDPM in a measurement technique called diffuse optical spectroscopic

imaging (DOSI).[35] DOSI measures absorption and scattering spectra (650 to 1000 nm) at each sample point. A clinical DOSI system is shown in Fig. 3(a), diagrammed in Fig. 3(b), and demonstrated in Fig. 3(c). The DOSI instrument is based on a commercial RF network analyzer (Agilent 8753E), which allows measurement of a continuous range of modulation frequencies from 50 to 1000 MHz.[36] Broadband FDPM allows one to sample PDW dispersion, where amplitude and phase are sensitive to both $\mu_a(\lambda)$ and $\mu'_s(\lambda)$ The RF output of the network analyzer is switched between six laser diodes, ranging from 650 to 860 nm, which deliver 10 to 30 mW of fiber-coupled average power to the tissue. The handpiece [Fig. 3(d)] holds the source fiber ends a set distance (adjustable from 22 to 34 mm) away from an integrated high-speed avalanche photodiode (APD) detector module (Hamamatsu C5658 with S-6045-03 APD). The APD signal is connected to the input channel of the network analyzer, where the amplitude and phase is measured in comparison to a reference line split from the source.

The FDPM component of the system measures $\mu_a(\lambda)$ and $\mu'_s(\lambda)$ at the laser diode wavelengths. Since phase and amplitude is influenced by the intrinsic response of the instrument (i.e., the RF cables, RF switches, and optical fibers), the amplitude and phase differences are compared to a standard reference material of known optical properties (e.g., silicone tissue phantom or intralipid solutions[37–39]). The resulting real and imaginary data (which can be transformed to amplitude and phase) are fit simultaneously using the P_1 diffusion approximation and semi-infinite boundary conditions as described above. Using Mie theory,[40–42] the scattering coefficients measured at the six laser diode wavelengths can be fit to a power law, which describes the scattering spectra $\mu'_s(\lambda)$ due to the wide distribution of scatters in the tissue:

$$\mu'_s(\lambda) = a\lambda^{-b}. \qquad (10)$$

Assuming a sampling across a range of wavelengths, this equation allows the full $\mu'_s(\lambda)$ spectra to be estimated from the six laser diode wavelengths.

The CW spectroscopy component of the DOSI system consists of a fiber-coupled tungsten-halogen white light source (Micropak HL2000-HP, Ocean Optics, Dunedin, Florida), and a spectrometer (B&W Tek, Inc. Model 611, Newark, Delaware) to obtain the broadband 650 to 1000 nm reflectance spectra. The instrument response is calibrated by using a Spectraflect®-coated diffuse reflectance standard (Labsphere, Inc, North Sutton, New Hampshire). Using the measured steady-state reflectance spectra and the scattering spectra obtained from the FDPM component, we return to diffusion theory and numerically calculate the corresponding broadband absorption spectra. Since both $\mu_a(\lambda)$ and $\mu'_s(\lambda)$ are measured over the full broadband 650 to 1000 nm range, Eq. (5) is applied over all measured wavelengths to fit the tissue chromophore concentrations at each measurement point.

The DOSI system presented here is a general-purpose, clinically compatible instrument for the measurement of broadband NIR optical properties in turbid media, but comes at a high cost ~50,000 to $75,000. The majority of the expense is due to the FDPM functionality, consisting of a network analyzer, laser driver, and bias network. Recent advances have allowed us to miniaturize these components in a printed circuit board (PCB).[43] The current miniaturized DOSI system consisting of four FDPM laser diodes and full broadband capability reduces many barriers to access for a clinical setting. The system
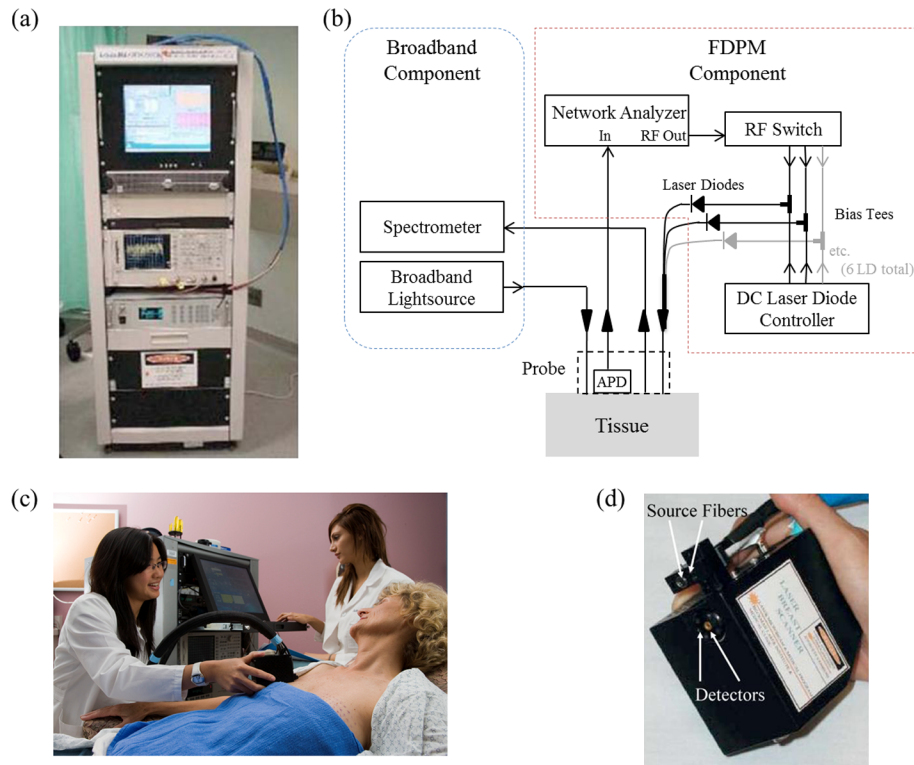
Fig. 3 Frequency domain photon migration instrumentation; (a) A clinical DOSI instrument, (b) a block diagram of the broadband DOSI instrument, (c) a subject measurement with the DOSI instrument, and (d) the handpiece placed in contact with the tissue.

provides equivalent accuracy to the Network Analyzer-based instrument and provides ∼5× faster measurement times at ∼10× less cost.

4 Spatial Frequency Domain Imaging

In SFDI, rather than launching temporally modulated light into the tissue and measuring the *t*-MTF, CW spatial patterns of light are projected on the tissue surface. This is sometimes referred to as structured-illumination. The resulting reflectance image is captured with an external, noncontact, nonscanning camera to measure the *s*-MTF. MTF is typically discussed in terms of the quality of optical lenses; in this case we are quantifying how the tissue modifies the incident light. It is possible to separate the individual contributions of absorption and scattering when the reciprocal of the spatial frequency is on the order of ∼1 to 10 times the transport scattering length. For example, at relatively high spatial frequencies (e.g., ∼0.5 mm^{-1}), the detected reflectance is dominated by shorter path length photons and minimally affected by absorption.

Like FDPM, the detected signal is fit to a model of light propagation in turbid media. At higher frequencies, the diffusion approximation breaks down and other models such as a Monte Carlo method must be used.[4] Multispectral measurements are obtained either by using multiple monochromatic sources (e.g., lasers or LEDs), or by using a broadband source with optical filters at the source or detector. The illumination pattern is captured at each wavelength with temporal resolution limited by the time required to project three phase patterns at a single frequency. For a two-color measurement (enough to recover ctO$_2$Hb and ctHHb), this has recently been reported to be as low as 0.5 s/frame.[44]

SFDI is related to multi-distance CW spectroscopy in which measurements at multiple source-detector separations are used in a model to estimate both absorption and reduced scattering coefficients.[45] In other words, multi-distance methods sample the spatial point spread function (*s*-PSF, see Fig. 1). Photons that are detected close to the source have propagated over distances that are much less than the absorption length and will be primarily affected by scattering. This can be compared to measurements made at distances far from the source which will be dependent on both scattering and absorption. These concepts are well established for point source measurements in the real domain using optical fibers[45] or a CCD[46] and in the frequency domain using imaging cameras.[47]

The first demonstration of an SFDI technique was in 1998 by Dögnitz and Wagnières.[48] A patterned glass plate placed in front of a filtered arc lamp defined the illumination structure, and reflectance was captured with a CCD camera. Although the intent of this device was not to map spatially varying optical properties or perform depth resolved imaging, it provided a non-contact approach for separating optical absorption from scattering. In 2005, we introduced an SFDI method for quantitative analysis, tomography, and imaging in turbid materials.[49] An SFDI instrument is shown in Fig. 4. A spatial light modulator, typically a digital micromirror (DMD) or liquid crystal on silicon (LCOS) device commonly found on commercial projectors and displays, is placed in front of a light source to create the projected patterns. Light sources should be monochromatic for wavelength-dependent optical property and chromophore recovery. Filtered white-light sources and LEDs are commonly employed. Cross-polarizers placed in front of the source and detector suppress superficial specular reflections and ensure that signals are derived from deep, multiply scattered photons.
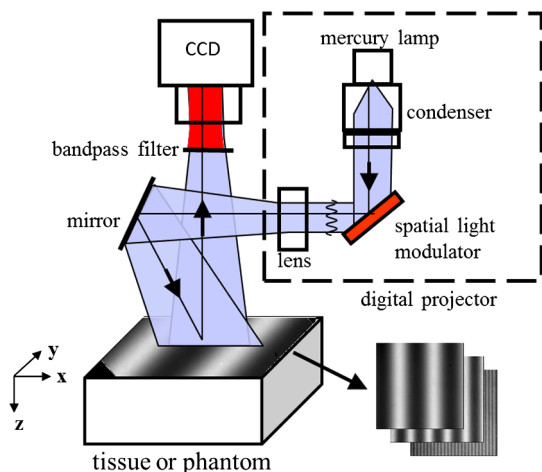
Fig. 4 An SFDI Instrument, reproduced with permission from Ref. 4.

A CCD camera captures tissue reflectance and determines the resolution of the optical property reconstruction. Each pixel provides unique reflectance information and is processed individually in the photon propagation model.

The sample/tissue is illuminated with a spatially varying pattern in one dimension of the form:

$$I_{IN} = \frac{S_0}{2}[1 + M_0 \cos(2\pi f_x x + \alpha)], \quad (11)$$

where S_0, M_0, f_x, and α are the illumination source intensity, modulation depth, spatial frequency, and spatial phase, respectively. The reflectance pattern intensity will have the form:

$$I_{OUT} = M_{AC}(x) \cos(2\pi f_x x + \alpha) + I_{DC}. \quad (12)$$

The reflected photon density standing wave amplitude will be modified by an envelope $M_{AC}(x)$ at frequency f_x, that is the product of the source intensity (I_0), the MTF of the illumination and imaging systems (instrument response, $\mathrm{MTF_{system}}$), and the MTF of the sample itself (R_d):

$$M_{AC}(x_i) = I_0 \cdot \mathrm{MTF_{system}}(x_i) \cdot R_d(x_i). \quad (13)$$

In practice, we measure $M_{AC}(x)$ by illuminating the same sinusoidal frequency at different phase offsets (0, 120, and 240 deg). The envelope function is extracted by using the equation, at each location x_i:

$$\begin{aligned} M_{AC}(x_i)|f_x = \frac{2^{1/2}}{3}\{&[I_1(x_i) - I_2(x_i)]^2 \\ &+ [I_2(x_i) - I_3(x_i)]^2 \\ &+ [I_3(x_i) - I_1(x_i)]^2\}^{1/2}. \quad (14) \end{aligned}$$

This operation is advantageous since it removes any measurement artifacts that are common to all three images (e.g., nonuniform illumination, ambient light, etc.).[4] Similar to FDPM, it is possible to calibrate for the instrument response by taking an SFDI measurement on a phantom of known optical phantoms using a model prediction of the diffuse reflectance. Each pixel in the image is treated independently, so reflectance and, therefore, optical properties calculated correspond to discrete

points. Figure 5 illustrates the data flow and processing steps of this imaging procedure.

Once the diffuse reflectance is recovered, a model of light propagation is applied to determine absorption and scattering properties. For the diffusion approximation to be valid, the reduced scattering coefficient must be much greater ($\geq 10\times$) than the absorption coefficient, and the analyzed source-detector separation at least three to four times the transport length $l^* = 1/(\mu_{tr}) = 1/(\mu_a + \mu_s')$. In the spatial frequency domain, the latter constraint dictates up to what spatial frequencies the diffusion approximation is valid. Since the spatial frequency analog to the transport length is the inverse of the transport spatial frequency $f_{x,tr}$, we estimate that the maximum spatial frequency for the diffusion approximation to be valid is $1/3 * \mu_{tr}$. In general, when approaching these constraints, the diffusion model overestimates reflectance at low spatial frequencies and underestimates reflectance at high frequencies.

To solve for $\mu_a(\lambda)$ and $\mu_s'(\lambda)$, as few as two spatial frequencies are required at each wavelength. Unlike the temporal frequency domain, where one can measure the phase and amplitude of the modulated signal, in the spatial frequency domain only magnitude/intensity of the reflectance is measured at each position. Thus one must choose spatial frequencies that provide sensitivity to absorption and scattering. In order to minimize acquisition time, it is convenient to measure a combination of CW illumination (DC) and a higher spatial frequency. Alternatively, reflectance from many different spatial frequencies can be fit to the light propagation model using a least squares technique. Note that the high frequency diffuse reflectance is much more sensitive to scattering than absorption, and vice-versa at low frequency. Qualitatively, scattering will cause the projected
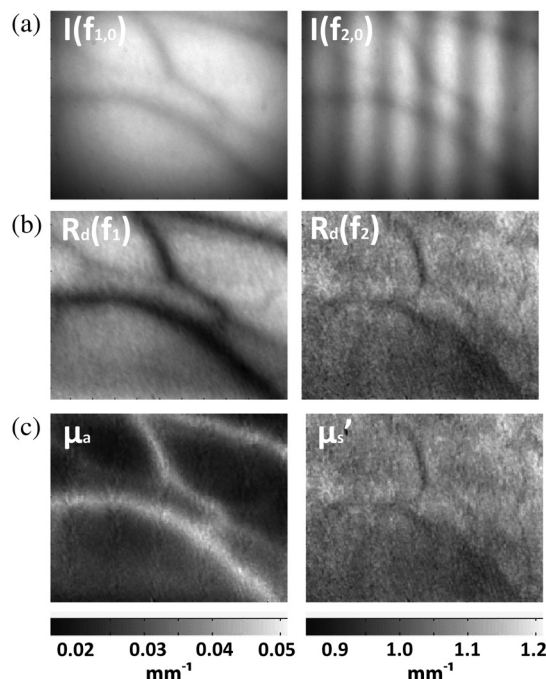

Fig. 5 Data flow and processing steps for SFDI image creation. (a) Multiple frequencies (f_x) are projected onto the sample, and remitted intensity I is captured. (b) Each illumination frequency is imaged at three phases, then demodulated and calibrated to yield R_d. (c) The R_d at each pixel is fit for and using a Monte Carlo light-transport model and lookup table to yield optical property maps. Reproduced with permission from Ref. 44.

pattern to appear blurred, while absorption will cause an overall average decrease in reflectance due to the lost photons.

In the simple illumination scheme above, we only consider a one-dimensional (1-D) pattern. More information can be gleaned, however, by varying the orientation of the illumination pattern. In tissues with well-defined anisotropic structure, such as muscle and brain, the light scattering direction will be modified. Therefore, by rotating the SFDI projection pattern and noting the angular dependence of blurring, it is possible to localize these anisotropic structures.[50]

Due to scattering, tissue acts as a low pass filter to spatially varying signals (Fig. 6), attenuating the higher spatial frequencies at greater depths. By selecting the correct spatial frequency, SFDI can be used to provide depth-resolved imaging. SFDI can provide multi-layer / 3-D tomographic reconstruction with <1 mm resolution at the surface and decreasing at greater depths up to several mm.[51–53] In addition to absorption and scattering, SFDI can also quantify fluorescent molecules with different optical filters on the source and camera.[54] Therefore, SFDI is a versatile technique that can map optical properties, quantify fluorescence, as well as provide tomographic reconstruction.

5 Applications

5.1 FDPM Application: Breast Oncology

FDPM offers deep tissue penetration and is highly sensitive to hemoglobin, water and lipids. FDPM provides noninvasive, quantitative functional information that is useful for a wide range of clinical applications where scatter-corrected absorption is required. In general, variations in tissue scattering should be considered in order to improve the accuracy of the measured absorption coefficient. This is particularly important in applications, such as oncology, where tumor-containing tissues have
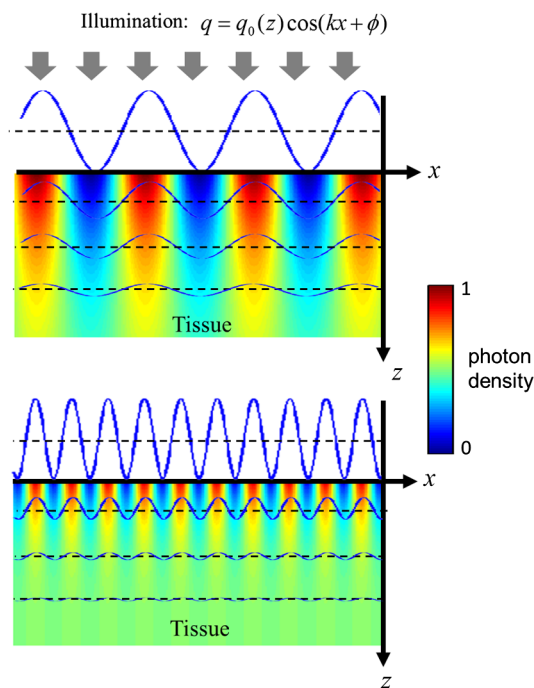
Fig. 6 Illustration of how tissue acts like a low-pass filter to spatially modulated illumination. Patterns with lower spatial frequencies propagate deeper into tissue.

spatially varying optical properties and frequent comparisons are made between patients.[55,56] FDPM methods have also been under investigation in the human brain[57–64] as well as muscles and joints.[65–67] Here we highlight breast oncology, which our group has explored in detail with the previously described DOSI instrument.

The human breast, in many ways, is an ideal tissue site for FDPM imaging. FDPM techniques have the capability to probe the entire tissue volume in either reflection or transmission geometries and accurately report major tissue chromophores and metabolic status. Our group performs DOSI imaging by using the probe shown in Fig. 3(d) to make measurements at multiple points on the breast. For colocation with anatomical features, and to assure repeat measurements are made at the same sites, a grid coordinate system centered at the nipple is drawn and recorded on a transparent film. Measurements are typically made moving the probe in 1 cm increments and tissue chromophores are mapped at each point to create an image of the entire measurement area.

DOSI is sensitive to normal variations in breast tissue composition caused by age and menstrual cycle and is able to distinguish between pre and postmenopausal women.[20,68–71] In a study of $N = 31$ women, it was found that premenopausal subjects ($N = 18$) have 2× mean total hemoglobin, 1.8× higher water concentration, and 50% lower lipid content than postmenopausal subjects ($N = 13$).[70] Furthermore, the study looked at the heterogeneity of the optical properties across the healthy breast, which is useful for determining the amount of contrast necessary to detect an abnormality. Because DOSI measures functional parameters that are related to microvasculature, cellular metabolism, and extracellular matrix, tumor-to-normal contrast can be well defined. Tumors possess abnormal vasculature, promote angiogenesis, and have a high rate of metabolism. Large tumors typically have necrotic centers due to insufficient perfusion. Proliferating tumors displace normal adipose tissue and have higher water content than surrounding normal tissue. All of these metrics are quantifiable using DOSI. Measurements of hemoglobin reflect tumor vasculature[72] and may be a direct indicator of angiogenesis.[73–75] Both water and lipid provide contrast in tumors compared to normal tissue.[76,77]

In one study, our group measured 58 palpable stage II/III breast tumors and the corresponding contralateral breast to identify optical contrast.[76] Fifty-seven subjects ranging in age from 18 to 81 (mean 50.5) were measured with a linescan over the tumor location, which was identified by mammography. Across the population, all of the basis chromophores including ctHHb, ctO$_2$Hb, water, and lipids exhibited statistically significant differences between malignant and normal tissue. The largest relative contrast, defined as the number of standard deviations difference between tumor and normal tissue, was observed in water (8.2), ctHHb (7.3), and lipid (−3.6). Water concentration was observed to correlate with the Nottingham-Bloom-Richardson histopathology score, perhaps due to increased cellularity and the relationship between tumor edema and grade.[78] As a result, we defined a tissue optical index (TOI), which summarizes the most significant elements of contrast in a single index:

$$\text{TOI} = \frac{\text{ctH}_2\text{O}}{\text{lipid}} \times \text{ctHHb}. \qquad (15)$$

TOI provided ~2× average contrast between the tumor and normal tissue. Figure 7 shows the DOSI chromophore maps from a

65-year-old subject with a right breast carcinoma measuring $19 \times 20 \times 32$ mm. There are significant increases in ctO_2Hb, ctHHb, and water, and a reduction in lipid over the area of the lesion. Note the uniformity of the chromophore concentrations in a mirrored region of the contralateral normal left breast.

Another DOSI contrast mechanism is related to probing the binding state of water. When water binds to protein, the NIR water absorption peak at ~960 nm is broadened and red-shifted.[79] Since DOSI provides a high-resolution broadband absorption spectrum, it is possible to detect these small shifts in the water peak. We captured this spectral change in an optical bound water index (BWI).[80] There are also additional tissue components that likely contribute to the NIR absorption contrast in breast tumors. These may take the form of proteins or hemoglobin by-products, modified absorption of lipid and hemoglobin due to binding states, or other local molecular interactions. A spectroscopic analysis of broadband DOSI data reveals that the spectra of these unknown "specific tumor components" (STC) can vary substantially in malignant versus benign tumors and potentially provide a basis for differential diagnosis.[81,82]

Neoadjuvant chemotherapy (NAC) is prescribed for breast cancer patients with locally advanced disease in an effort to shrink or eliminate the primary tumor as well as improve breast tissue conservation during surgical resection. A patient exhibiting a pathological complete response (pCR) has no histopathological evidence of malignancy at surgery and this result correlates with favorable overall survival for many breast cancer subtypes.[83,84] In contrast, the 8% to 20% of patients who do not respond well to NAC[85,86] continue to experience progressive disease and have reduced overall survival.[85] NAC response is usually monitored with palpation, ultrasound, and mammography, but these methods have been shown to be inadequate for predicting pathological response.[87] These techniques only measure the size of the tumor, which is predicated on underlying functional changes. Because of its sensitivity to underlying functional changes in the tumor, DOSI may be a safe, effective modality for predicting chemotherapy response, both prior to and early during treatment.

Our group has been using DOSI to measure breast tumors in subjects undergoing NAC for nearly 10 years.[88–95] In the largest study of NAC DOI to date, we measured 34 patients with 36 confirmed malignancies (two had bilateral disease).[93] The subjects were given a variety of chemotherapy regimens as recommended by their oncologists, and DOSI was acquired at baseline, midway through therapy, and before surgery. Over the entire group, significant changes were noted in both tumor and normal regions. Tumor region values approached

normal regions with lower ctH_2O, higher lipid concentration, and lower ctHHb and ctO_2Hb. This resulted in a 59% drop in the tissue optical index, TOI [Eq. (15)]. The observed changes agree with known tumor biology. The decreased oxy-, deoxy-, and total hemoglobin levels are consistent with diminished perfusion, metabolism, and vessel density, respectively, a signature of NAC response.[96] The increase in lipid suggests the return of normal adipose to the region surrounding the tumor. Similarly, decreasing water content reflects a loss of tumor cellularity and edema. These changes have also been noted by other researchers.[97–102]

The change in DOSI values were compared between pCR ($N = 11$) and nonpCR ($N = 25$) groups to assess whether DOSI can predict pathological response early during NAC. At the treatment midpoint, the ratio of the TOI between tumor and normal tissue dropped $47 \pm 8\%$ for pCR and $20 \pm 5\%$ for nonpCR subjects. The results show that pCR subjects are likely to have a greater response indicated by TOI earlier in NAC treatment than the non-pCR subjects. This hypothesis is presently being tested and verified in a multi-site clinical study by the American College of Radiology Imaging Network (ACRIN-6691). Figure 8 shows the preliminary data for one of these subjects. This subject exhibited a dramatic reduction in TOI at midpoint (10×) and continued to achieve pCR.

We have also observed changes in DOSI signatures as early as one day after beginning treatment that can predict pathological response.[94] In a study of 23 NAC patients who were measured multiple times during the first week of therapy, it was discovered that all responding (partial response or pCR) tumors showed a spike (44% increase) in ctO_2Hb on the first day following treatment, which decreased rapidly on day two. For comparison, non-pCR subjects exhibited a 25% reduction in ctO_2Hb the first day. Analysis of the normal region showed no simultaneous statistically significant difference in chromophore values between responders and non-pCR. We hypothesize that this early vascular reaction is characteristic of an acute, systemic inflammatory response induced by cell damage/death. The lack of reaction in nonresponders may be due to a higher proportion of chemoresistant or nonimmunostimulatory tumor cells and/or less reactive tumor vasculature.

5.2 SFDI Applications

SFDI is uniquely suited to applications that require wide-field measurement of optical properties at a shallow penetration depth. In humans, this includes applications related to skin
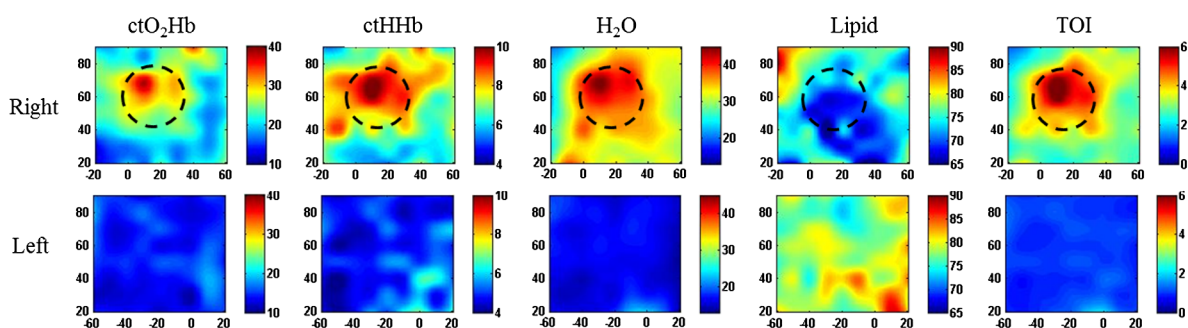
Fig. 7 DOSI images of chromophore values of a 65-year-old subject with carcinoma of the right breast, measuring $19 \times 20 \times 32$ mm by ultrasound. The approximate tumor location is indicated by the black circle, confirmed by palpation. Measurements are taken in a grid pattern every 10 mm and interpolated to create these image maps.
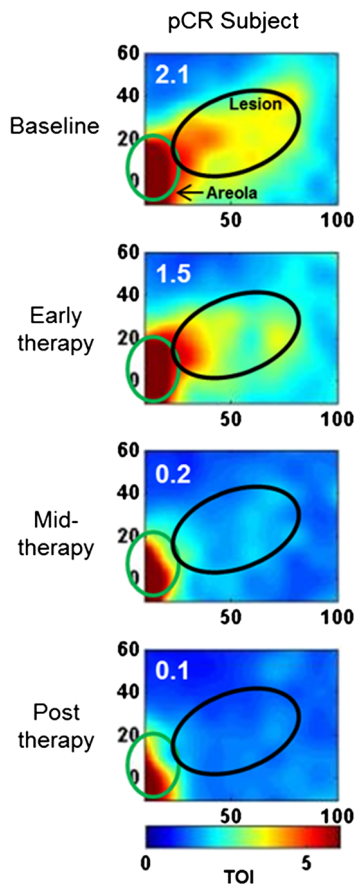
Fig. 8 Longitudinal DOSI measurements of a breast carcinoma during neoadjuvant chemotherapy (NAC) treatment. After surgery, this patient was confirmed to have no evidence of residual cancer and achieved a pathologic complete response (pCR). The inset value indicates the tumor to normal optical contrast in TOI.

imaging.[52] SFDI penetration depth is also applicable to preclinical models of brain injury,[103] stroke,[104] cortical spreading depression,[105] and Alzheimer's disease (AD).[106] It is also capable of providing 3D tomographic reconstruction,[51,53,107] and fluorescence imaging.[54]

5.2.1 Preclinical models of neurological disease

SFDI is useful in neurological imaging because it provides a noncontact, high-resolution, wide-field measurement of intrinsic signals. In addition to quantitative measurements of absorption-derived chromophore concentrations, SFDI reports tissue scattering parameters that can reveal structural contrast. This may include alterations due to tissue swelling, as well as changes in cell and white matter due to injury and degenerative disease. Because SFDI is a camera-based method that quantifies both absorption and scattering in a scan-free, noncontact geometry, it can be extended to clinical neurological imaging studies in operative settings.

During ischemic stroke blockage of a main artery supplying the brain starves cells for oxygen, eventually leading to cell death. As this occurs, there are massive changes in the regional concentrations of ctO_2Hb, $ctHHb$, water, and stO_2, which can be quantified with SFDI. In a preclinical study of ischemic stroke, Abookasis et al. used SFDI to image the left parietal somatosensory barrel cortex on rats through a thinned skull (150 μm).[104]
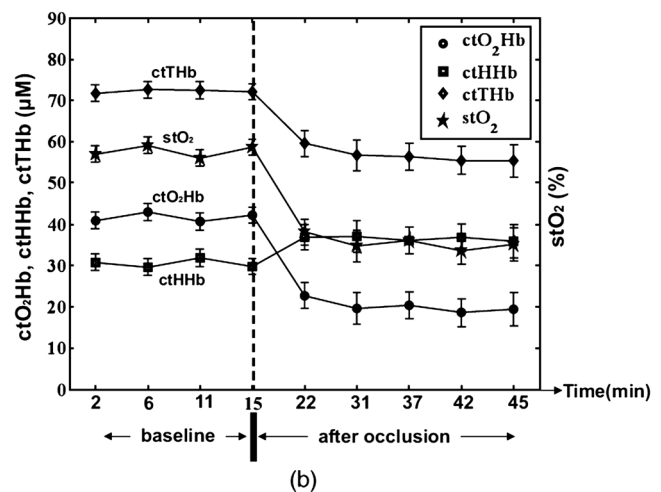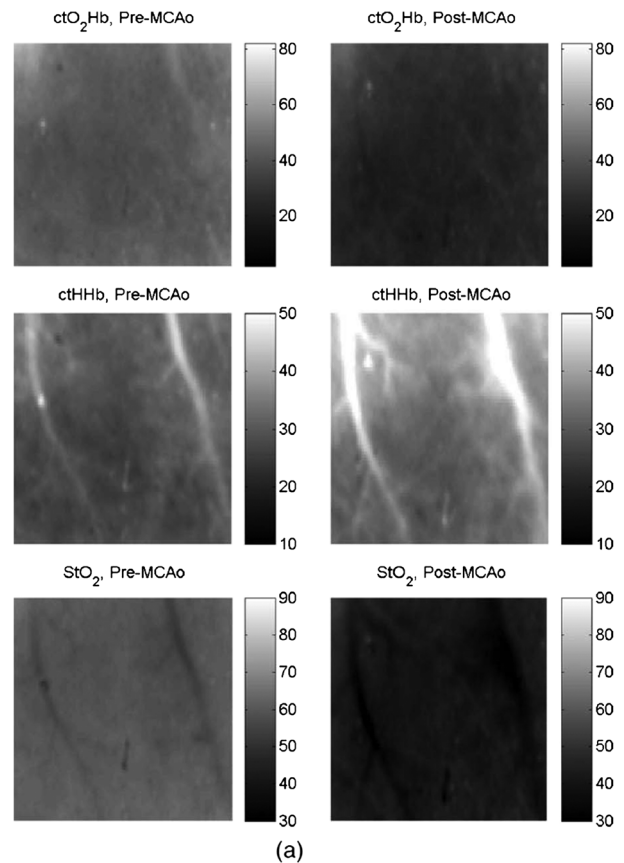
Fig. 9 Representative SFDI images (6 × 6 mm) of the barrel cortex of a rat undergoing a middle cerebral artery occlusion (MCAo), a model of ischemic stroke. (a) Chromophore maps pre and postMCAo. (b) Time course of cerebral hemodynamics from the barrel cortex as analyzed from these images. The error bars give the standard error of all pixels in a region of interest. Reproduced with permission from Ref. 104.

After imaging began, ischemia was induced by cauterizing or ligating the middle cerebral artery. Imaging was started 15 min after the occlusion and continued for 1 h. Significant changes in optical absorption occurred that were attributed to a 17% increase in $ctHHb$, 45% decrease in ctO_2Hb, 23% decrease in $ctTHb$, and a 21% reduction in stO_2 (Fig. 9). Concurrent decreases in ctO_2Hb and increases in $ctHHb$ were due to continued metabolic activity in the context of reduced hemoglobin

delivery. The reduced scattering coefficient increased post-occlusion, possibly due to swelling-induced changes in the density of light scatterers.

The ability of SFDI to quantify neural tissue function is further demonstrated in a study by Lin et al.[106], which examined brain alterations in a transgenic mouse model of AD. Clinical imaging modalities such as fMRI, PET, and SPECT have revealed reduced vascular reactivity in AD patients in response to vasodilation challenges. It is hypothesized that decreased vascular response to hypoxia leads to local hypoxic stress and production of amyloid-beta, the deposits of which are associated with AD. The aim of the study was to examine neurological differences in a transgenic mouse AD model and age-matched controls. SFDI was performed by removing the skin and imaging through intact skull. A wide-band, 17-wavelength SFDI measurement was taken at baseline, and two-wavelength measurements were recorded continuously (every 15 s) during successive hyperoxia (100% O_2) inhalation challenges. There were significant differences between normal and AD groups at baseline (Fig. 10), including 68% greater water content, 27% lower ctTHb, and 17% lower stO_2 in the AD mice. Scattering values were also significantly higher (13% to 26%) in the AD mice, which may be consistent with edema. As a result of the inhalation challenge, the AD mice were found to exhibit a 2× to 3× slower response, and the magnitude of the change in ctO_2Hb, $ctHHb$, and stO_2 was significantly attenuated. Overall, the results showed impaired vascular perfusion and reactivity in the AD mice.

5.2.2 SFDI in skin imaging

The high lateral resolution and shallow depth penetration makes SFDI ideal for noninvasive skin imaging in humans. Vascular structures in the dermis and subcutaneous layers contain a strong, detectable NIR signal. In addition, SFDI is sensitive to porphyrin fluorescence, which is of interest in photodynamic therapy for skin cancer.[108] Human applications already being investigated include wound and flap healing,[109] burn assessment,[110] and measuring vascular reactivity.[44]

Researchers recently demonstrated the first human reconstructive flap application of SFDI at Beth Israel Deaconess Medical Center.[109] For women undergoing breast reconstruction after mastectomy, a common procedure requires transferring a tissue flap, which may include skin, fat, and muscle to cover the breast mound. This flap tissue will cover and provide support for a breast implant, and while the procedure is usually successful, a late flap failure (more than 6 h after surgery) will result in loss of the tissue transplant altogether. Clinical observations based on color, temperature, skin turgor, capillary refill time, and bleeding time after pinprick are the most common practice for flap monitoring. The success of the flap is based on the restoration of the blood supply to the tissue. Both blood volume and tissue oxygenation can be measured directly with SFDI over the entire area of the flap.

Preclinical models of flap transfer have also been monitored using SFDI in rats.[111,112] In one study, bilateral groin skin flaps with a separate but singular vascular supply based on the inferior epigastric vessels were created.[111] An external clamp for inducing an occlusion in addition to a cannula inserted into the femoral artery provided the ability to control flap perfusion. A clamp was placed for 2 h to induce either a venous or arterio-venous occlusion, after which hypertonic hyperoncotic saline solution was administered to induce necrosis. Control flaps were also occluded, but saline solution was instead administered afterwards as a control. During the occlusion, significant changes in ctO_2Hb, $ctHHb$, ctTHb, and StO_2 were observable compared to the intact tissue (Fig. 11). After the occlusion was released, surviving flaps readily showed
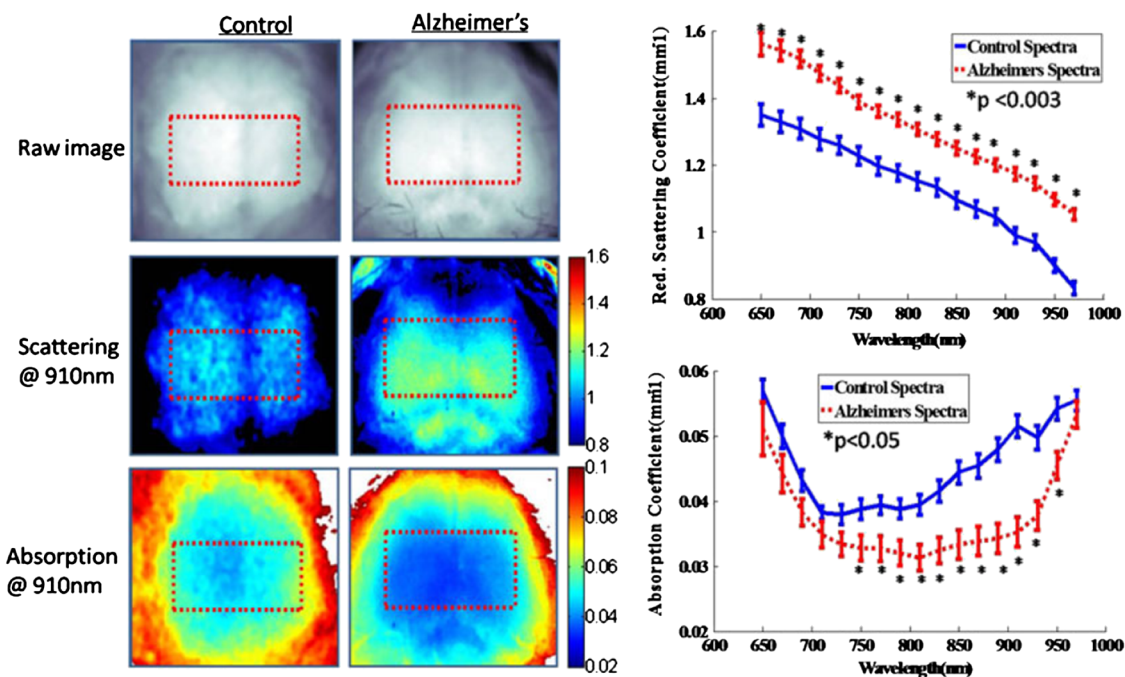
Fig. 10 Representative optical property maps of the brain in a mouse model of Alzheimer's disease taken with SFDI *in vivo* through intact skull. Pixel values in the ROI were averaged for each mouse and wavelength-dependent reduced scattering and absorption coefficient spectra were plotted for control and transgenic mice. Reproduced with permission from Ref. 106.
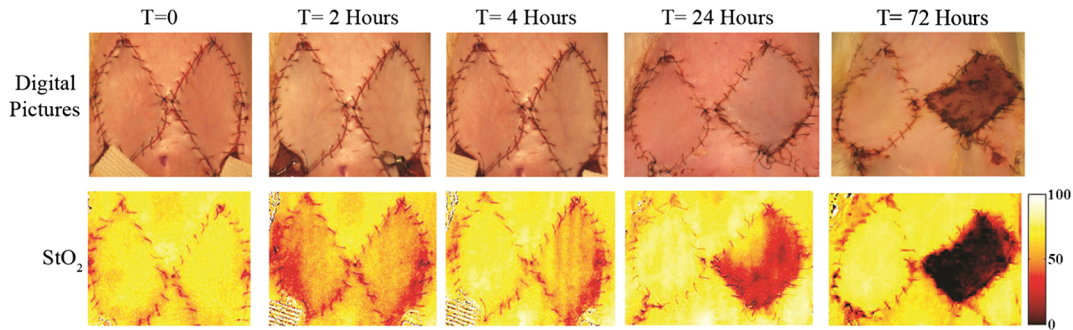
Fig. 11 SFDI images of StO$_2$ and corresponding digital images of a rat model of flap healing. The baseline image is shown at $T = 0$, which was followed by 2 h of ischemia and two additional hours of treatment. The flap on the left in each image represents the control flap that was treated with normal saline after 2 h of ischemia and ultimately survived. The right flap in each image represents the experimental flap that was treated with hypertonic-hyperoncotic saline after 2 h of ischemia and eventually became necrotic within 24 to 48 h. This figure was reproduced with permission from data originally published in Ref. 111.

normalized perfusion with oxygen saturation returning to baseline. ctO$_2$Hb increased rapidly within 45 min of reperfusion, whereas flaps that did not eventually survive exhibited no such increase as stO$_2$ continued to decline. The study showed that SFDI can predict flap failure at very early timepoints in these animal models.

When a multi-layer model is applied,[52,113,114] SFDI measurements from the skin surface can distinguish between the epidermis, dermis, and subcutaneous tissue. This is important because the epidermis contains melanin, an optical absorber, while hemoglobin is located in the dermis.

6 Summary and Future Perspectives

Diffuse optical methods provide a relatively inexpensive, portable, and flexible platform for determining tissue structure and molecular composition *in vivo*. Quantitative measurements are obtained by separating absorption from scattering using spatially or temporally modulated light and model-based analyses. This gives DOI the ability to measure endogenous chromophores, such as the tissue concentration of oxy- and deoxy-hemoglobin, lipid, and water, and provide functional information on tissue perfusion and metabolism.

There are many strategies for further improvements in contrast, sensitivity and specificity by combining DOI with molecular-targeted exogenous absorption and fluorescence contrast agents.[115,116] Targeted probes can potentially improve DOI spatial localization and enhance functional information content. Spectrally broadband measurements of multiple endogenous and exogenous chromophores can reveal relationships between intrinsic biochemical composition and specific molecular pathways. Quantitative determination of tissue optical properties can facilitate more accurate imaging by accounting for intrinsic tissue absorption and scattering properties that are known to distort the spectral signatures of exogenous probes.

Quantitative DOI methods are most advantageous when assessing physiologically dynamic, heterogeneous tissues such as wounds, injuries, and tumors. Under these conditions, model-based techniques can be used to determine absolute values of tissue optical and physiological properties. Unlike trend monitoring that is performed with relative CW-NIRS measurements, quantitative DOI methods can be used to compare patients and monitor therapies over extended periods. Because they are relatively inexpensive, have unique information content, and can be deployed at the bedside, DOI is expected grow in the general area of personalized medicine. Important emerging applications include image guided surgery, monitoring neurologic function in anesthesiology and brain injury, improving oncologic therapy, and detecting breast cancer in high-risk patients who do not benefit from mammography. As DOI technologies mature, a major continuing challenge will be technology standardization which is necessary to utilize validated optical endpoints as a means for optimizing and predicting clinical outcome.

References

1. S. L. Jacques and B. W. Pogue, "Tutorial on diffuse light transport," *J. Biomed. Opt.* **13**(4), 041302 (2008).
2. C. E. Elwell and C. E. Cooper, "Making light work: illuminating the future of biomedical optics," *Philos. T. Roy. Soc. A* **369**(1955), 4358–4379 (2011).

3. M. S. Patterson, B. Chance, and B. C. Wilson, "Time resolved reflectance and transmittance for the non-invasive measurement of tissue optical properties," *Appl. Opt.* **28**(12), 2331–2336 (1989).

4. D. J. Cuccia et al., "Quantitation and mapping of tissue optical properties using modulated imaging," *J. Biomed. Opt.* **14**(2), 024012 (2009).

5. S. R. Arridge, "Optical tomography in medical imaging," *Inverse Probl.* **15**(2), R41–R93 (1999).

6. S. R. Arridge, "Methods in diffuse optical imaging," *Philos. T. Roy. Soc. A* **369**(1955), 4558–4576 (2011).

7. H. Dehghani et al., "Numerical modelling and image reconstruction in diffuse optical tomography," *Philos. T. Roy. Soc. A* **367**(1900), 3073–3093 (2009).

8. A. P. Gibson, J. C. Hebden, and S. R. Arridge, "Recent advances in diffuse optical imaging," *Phys. Med. Biol.* **50**(4), R1–R43 (2005).

9. A. Ishimaru, "Theory and application of wave propagation and scattering in random media," *Proc. IEEE* **65**(7), 1030–1061 (1977).

10. A. Ishimaru, *Wave Propagation and Scattering in Random Media*, Academic Press, New York (1978).

11. A. D. Kim, "Transport theory for light propagation in biological tissue," *J. Opt. Soc. Am. A* **21**(5), 820–827 (2004).

12. L. V. Wang and H.-I. Wu, *Biomedical Optics: Principles and Imaging*, John Wiley & Sons Inc., Hoboken, New Jersey (2007).

13. A. Yodh and B. Chance, "Spectroscopy and imaging with diffusing light," *Phys. Today* **48**(3), 34–40 (1995).

14. A. E. Cerussi and B. J. Tromberg, "Photon migration spectroscopy frequency-domain techniques," in *Biomedical Photonics Handbook*, T. Vo-Dinh, ed., CRC Press, Boca Raton, Florida (2003).

15. J. B. Fishkin et al., "Gigahertz photon density waves in a turbid medium: theory and experiments," *Phys. Rev. E* **53**(3), 2307–2319 (1996).

16. R. C. Haskell et al., "Boundary conditions for the diffusion equation in radiative transfer," *J. Opt. Soc. Am. A* **11**(10), 2727–2741 (1994).

17. J. B. Fishkin and E. Gratton, "Propagation of photon-density waves in strongly scattering media containing an absorbing semi-infinite plane bounded by a straight edge," *J. Opt. Soc. Am. A, Opt. Image Sci.* **10**(1), 127–140 (1993).

18. W. G. Zijlistra, A. Buursma, and O. W. V. Assendelft, *Visible and Near Infrared Absorption Spectra of Human and Animal Haemoglobin: Determination and Application*, VSP, Utrecht (2000).

19. R. Cubeddu et al., "Effects of the menstrual cycle on the red and near-infrared optical properties of the human breast," *Photochem. Photobiol.* **72**(3), 383–391 (2000).

20. A. E. Cerussi et al., "Spectroscopy enhances the information content of optical mammography," *J. Biomed. Opt.* **7**(1), 60–71 (2002).

21. R. L. van Veen et al., "Determination of visible near-IR absorption coefficients of mammalian fat using time- and spatially resolved diffuse reflectance and transmission spectroscopy," *J. Biomed. Opt.* **10**(5), 054004 (2005).

22. L. O. Svaasand and B. J. Tromberg, "On the properties of optical waves in turbid media," *Time-Resolved Spectroscopy and Imaging of Tissues* **1525**, 41–51 (1991).

23. R. F. Bonner et al., "Model for photon migration in turbid biological media," *J. Opt. Soc. Am. A* **4**(3), 423–432 (1987).

24. B. Chance et al., "Comparison of time-resolved and time-unresolved measurements of deoxyhemoglobin in brain," *Proc. Natl. Acad. Sci. U.S.A.* **85**(14), 4971–4975 (1988).

25. D. T. Delpy et al., "Estimation of optical pathlength through tissue from direct time of flight measurement," *Phys. Med. Biol.* **33**(12), 1433–1442 (1988).

26. J. R. Lakowicz and K. Berndt, "Frequency-domain measurements of photon migration in tissues," *Chem. Phys. Lett.* **166**(3), 246–252 (1990).

27. J. B. Fishkin et al., "Diffusion of intensity-modulated near-infrared light in turbid media," *Time-Resolved Spectroscopy and Imaging of Tissues* **1431**, 122–135 (1991).

28. M. S. Patterson et al., "Frequency-domain reflectance for the determination of the scattering and absorption properties of tissue," *Appl. Opt.* **30**(31), 4474–4476 (1991).

29. E. M. Sevick et al., "Quantitation of time- and frequency-resolved optical spectra for the determination of tissue oxygenation," *Anal. Biochem.* **195**(2), 330–351 (1991).

30. B. J. Tromberg et al., "Optical property measurements in turbid media using frequency-domain photon migration," *Time-Resolved Spectroscopy and Imaging of Tissues* **1525**, 52–58 (1991).

31. J. M. Schmitt, A. Knüttel, and J. R. Knutson, "Interference of diffusive light waves," *J. Opt. Soc. Am. A* **9**(10), 1832–1843 (1992).

32. M. A. O'Leary et al., "Refraction of diffuse photon density waves," *Phys. Rev. Lett.* **69**(18), 2658–2661 (1992).

33. D. A. Boas et al., "Scattering and wavelength transduction of diffuse photon density waves," *Phys. Rev. E* **47**(5), R2999–R3002 (1993).

34. B. J. Tromberg et al., "Properties of photon density waves in multiple-scattering media," *Appl. Opt.* **32**(4), 607–616 (1993).

35. F. Bevilacqua et al., "Broadband absorption spectroscopy in turbid media by combined frequency-domain and steady-state methods," *Appl. Opt.* **39**(34), 6498–6507 (2000).

36. T. H. Pham et al., "Broad bandwidth frequency domain instrument for quantitative tissue optical spectroscopy," *Rev. Sci. Instrum.* **71**(6), 2500–2513 (2000).

37. A. E. Cerussi et al., "Tissue phantoms in multicenter clinical trials for diffuse optical technologies," *Biomed. Opt. Express* **3**(5), 966–971 (2012).

38. R. Cubeddu et al., "A solid tissue phantom for photon migration studies," *Phys. Med. Biol.* **42**(10), 1971–1979 (1997).

39. B. W. Pogue and M. S. Patterson, "Review of tissue simulating phantoms for optical spectroscopy, imaging and dosimetry," *J. Biomed. Opt.* **11**(4), 041102 (2006).

40. R. Graaff et al., "Reduced light-scattering properties for mixtures of spherical particles: a simple approximation derived from Mie calculations," *Appl. Opt.* **31**(10), 1370–1376 (1992).

41. J. R. Mourant et al., "Mechanisms of light scattering from biological cells relevant to noninvasive optical-tissue diagnostics," *Appl. Opt.* **37**(16), 3586–3593 (1998).

42. J. R. Mourant et al., "Predictions and measurements of scattering and absorption over broad wavelength ranges in tissue phantoms," *Appl. Opt.* **36**(4), 949–957 (1997).

43. K.-S. No et al., "Design and testing of a miniature broadband frequency domain photon migration instrument," *J. Biomed. Opt.* **13**(5), 050509 (2008).

44. A. Mazhar et al., "Wavelength optimization for rapid chromophore mapping using spatial frequency domain imaging," *J. Biomed. Opt.* **15**(6), 061716 (2010).

45. T. J. Farrell, M. S. Patterson, and B. Wilson, "A diffusion theory model of spatially resolved, steady-state diffuse reflectance for the noninvasive determination of tissue optical properties in vivo," *Med. Phys.* **19**(4), 879–888 (1992).

46. A. Kienle et al., "Spatially resolved absolute diffuse reflectance measurements for noninvasive determination of the optical scattering and absorption coefficients of biological tissue," *Appl. Opt.* **35**(13), 2304–2314 (1996).

47. T. H. Pham et al., "Quantifying the optical properties and chromophore concentrations of turbid media by chemometric analysis of hyperspectral diffuse reflectance data collected using a Fourier interferometric imaging system," *Appl. Spectrosc.* **55**(8), 1035–1045 (2001).

48. N. Dögnitz and G. Wagnières, "Determination of tissue optical properties by steady-state spatial frequency-domain reflectometry," *Laser. Med. Sci.* **13**(1), 55–65 (1998).

49. D. J. Cuccia et al., "Modulated imaging: quantitative analysis and tomography of turbid media in the spatial-frequency domain," *Opt. Lett.* **30**(11), 1354–1356 (2005).

50. S. D. Konecky et al., "Imaging scattering orientation with spatial frequency domain imaging," *J. Biomed. Opt.* **16**(12), 126001 (2011).

51. S. D. Konecky et al., "Quantitative optical tomography of sub-surface heterogeneities using spatially modulated structured light," *Opt. Express* **17**(17), 14780–14790 (2009).

52. J. R. Weber et al., "Noncontact imaging of absorption and scattering in layered tissue using spatially modulated structured light," *J. Appl. Phys.* **105**(10), 102028 (2009).

53. S. D. Konecky et al., "Spatial frequency domain tomography of protoporphyrin IX fluorescence in preclinical glioma models," *J. Biomed. Opt.* **17**(5), 056008 (2012).

54. A. Mazhar et al., "Structured illumination enhances resolution and contrast in thick tissue fluorescence imaging," *J. Biomed. Opt.* **15**(1), 010506 (2010).

55. B. J. Tromberg et al., "Assessing the future of diffuse optical imaging technologies for breast cancer management," *Med. Phys.* **35**(6), 2443–2451 (2008).
56. B. J. Tromberg et al., "Non-invasive in vivo characterization of breast tumors using photon migration spectroscopy," *Neoplasia* **2**(1/2), 26–40 (2000).
57. E. Gratton et al., "Measurements of scattering and absorption changes in muscle and brain," *Philos. T. Roy. Soc. B* **352**(1354), 727–735 (1997).
58. F. Bevilacqua et al., "In vivo local determination of tissue optical properties: applications to human brain," *Appl. Opt.* **38**(22), 4939–4950 (1999).
59. J. Choi et al., "Noninvasive determination of the optical properties of adult brain: near-infrared spectroscopy approach," *J. Biomed. Opt.* **9**(1), 221–229 (2004).
60. B. Zhu et al., "Diffuse optical imaging of brain activation to joint attention experience," *Behav. Brain Res.* **202**(1), 32–39 (2009).
61. N. Roche-Labarbe et al., "Noninvasive optical measures of CBV, StO$_2$, CBF index, and rCMRO$_2$ in human premature neonates' brains in the first six weeks of life," *Hum. Brain Mapp.* **31**(3), 341–352 (2010).
62. L. Meng et al., "Effect of phenylephrine and ephedrine bolus treatment on cerebral oxygenation in anaesthetized patients," *Brit. J. Anaesth.* **107**(2), 209–217 (2011).
63. P.-Y. Lin et al., "Regional and hemispheric asymmetries of cerebral hemodynamic and oxygen metabolism in newborns," *Cereb. Cortex* (2012).
64. L. Meng et al., "Head-up tilt and hyperventilation produce similar changes in cerebral oxygenation and blood volume: an observational comparison study using frequency-domain near-infrared spectroscopy," *Can. J. Anaesth.* **59**(4), 357–365 (2012).
65. V. Quaresima et al., "Difference in leg muscle oxygenation during treadmill exercise by a new near-infrared frequency-domain oximeter," *Time-Resolved Spectroscopy and Imaging of Tissues* **3194**, 116–120 (1998).
66. U. J. Netz, J. Beuthan, and A. H. Hielscher, "Multipixel system for gigahertz frequency-domain optical imaging of finger joints," *Rev. Sci. Instrum.* **79**(3), 034301 (2008).
67. D. Jakubowski et al., "Quantitative absorption and scattering spectra in thick tissues using broadband diffuse optical spectroscopy," in *Biomedical Optical Imaging*, J. G. Fujimoto and D. L. Farkas, Eds., pp. 330–355, Oxford University Press, New York (2009).
68. A. E. Cerussi et al., "Sources of absorption and scattering contrast for near-infrared optical mammography," *Acad. Radiol.* **8**(3), 211–218 (2001).
69. N. Shah et al., "Noninvasive functional optical spectroscopy of human breast tissue," *Proc. Natl. Acad. Sci. U.S.A.* **98**(8), 4420–4425 (2001).
70. N. Shah et al., "Spatial variations in optical and physiological properties of healthy breast tissue," *J. Biomed. Opt.* **9**(3), 534–540 (2004).
71. B. J. Tromberg et al., "Imaging in breast cancer: diffuse optics in breast cancer: detecting tumors in pre-menopausal women and monitoring neoadjuvant chemotherapy," *Breast Cancer Res.* **7**(6), 279–285 (2005).
72. H. Liu et al., "Influence of blood vessels on the measurement of hemoglobin oxygenation as determined by time-resolved reflectance spectroscopy," *Med. Phys.* **22**(8), 1209–1217 (1995).
73. B. W. Pogue et al., "Quantitative hemoglobin tomography with diffuse near-infrared spectroscopy: pilot results in the breast," *Radiology* **218**(1), 261–266 (2001).
74. B. J. Tromberg et al., "Non-invasive in vivo characterization of breast tumors using photon migration spectroscopy," *Neoplasia* **2**(1–2), 26–40 (2000).
75. Q. Zhu et al., "Utilizing optical tomography with ultrasound localization to image heterogeneous hemoglobin distribution in large breast cancers," *Neoplasia* **7**(3), 263–270 (2005).
76. A. Cerussi et al., "In vivo absorption, scattering, and physiologic properties of 58 malignant breast tumors determined by broadband diffuse optical spectroscopy," *J. Biomed. Opt.* **11**(4), 044005 (2006).
77. P. Taroni et al., "Clinical trial of time-resolved scanning optical mammography at 4 wavelengths between 683 and 975 nm," *J. Biomed. Opt.* **9**(3), 464–473 (2004).
78. O. Tervonen et al., "Diffuse "fibrillary" astrocytomas: correlation of MRI features with histopathologic parameters and tumor grade," *Neuroradiology* **34**(3), 173–178 (1992).
79. L. Pauling, *The Nature of the Chemical Bond*, Cornell University Press, Ithaca, New York (1960).
80. S. H. Chung et al., "In vivo water state measurements in breast cancer using broadband diffuse optical spectroscopy," *Phys. Med. Biol.* **53**(23), 6713–6727 (2008).
81. S. Kukreti et al., "Intrinsic tumor biomarkers revealed by novel double-differential spectroscopic analysis of near-infrared spectra," *J. Biomed. Opt.* **12**(2), 020509 (2007).
82. S. Kukreti et al., "Characterization of metabolic differences between benign and malignant tumors: high-spectral-resolution diffuse optical spectroscopy," *Radiology* **254**(1), 277–284 (2010).
83. B. Fisher et al., "Effect of preoperative chemotherapy on the outcome of women with operable breast cancer," *J. Clin. Oncol.* **16**(8), 2672–2685 (1998).
84. E. R. Fisher et al., "Pathobiology of preoperative chemotherapy: findings from the National Surgical Adjuvant Breast and Bowel (NSABP) protocol B-18," *Cancer* **95**(4), 681–695 (2002).
85. A. S. Caudle et al., "Predictors of tumor progression during neoadjuvant chemotherapy in breast cancer," *J. Clin. Oncol.* **28**(11), 1821–1828 (2010).
86. P. Rastogi et al., "Preoperative chemotherapy: updates of National Surgical Adjuvant Breast and Bowel Project Protocols B-18 and B-27," *J. Clin. Oncol.* **26**(5), 778–785 (2008).
87. A. A. Tardivon et al., "Monitoring therapeutic efficacy in breast carcinomas," *Eur. Radiol.* **16**(11), 2549–2558 (2006).
88. D. B. Jakubowski et al., "Monitoring neoadjuvant chemotherapy in breast cancer using quantitative diffuse optical spectroscopy: a case study," *J. Biomed. Opt.* **9**(1), 230–238 (2004).
89. N. Shah et al., "Combined diffuse optical spectroscopy and contrast-enhanced magnetic resonance imaging for monitoring breast cancer neoadjuvant chemotherapy: a case study," *J. Biomed. Opt.* **10**(5), 051503 (2005).
90. A. Cerussi et al., "Predicting response to breast cancer neoadjuvant chemotherapy using diffuse optical spectroscopy," *Proc. Natl. Acad. Sci. U.S.A.* **104**(10), 4014–4019 (2007).
91. C. Zhou et al., "Diffuse optical monitoring of blood flow and oxygenation in human breast cancer during early stages of neoadjuvant chemotherapy," *J. Biomed. Opt.* **12**(5), 051903 (2007).
92. A. E. Cerussi et al., "Frequent optical imaging during breast cancer neoadjuvant chemotherapy reveals dynamic tumor physiology in an individual patient," *Acad. Radiol.* **17**(8), 1031–1039 (2010).
93. A. E. Cerussi et al., "Diffuse optical spectroscopic imaging correlates with final pathological response in breast cancer neoadjuvant chemotherapy," *Philos. T. Roy. Soc. A* **369**(1955), 4512–4530 (2011).
94. D. Roblyer et al., "Optical imaging of breast cancer oxyhemoglobin flare correlates with neoadjuvant chemotherapy response one day after starting treatment," *Proc. Natl. Acad. Sci. U.S.A.* **108**(35), 14626–14631 (2011).
95. Y. Santoro et al., "Breast cancer spatial heterogeneity in near-infrared spectra and the prediction of neoadjuvant chemotherapy response," *J. Biomed. Opt.* **16**(9), 097007 (2011).
96. A. Makris et al., "Reduction in angiogenesis after neoadjuvant chemoendocrine therapy in patients with operable breast carcinoma," *Cancer* **85**(9), 1996–2000 (1999).
97. H. Soliman et al., "Functional imaging using diffuse optical spectroscopy of neoadjuvant chemotherapy response in women with locally advanced breast cancer," *Clin. Cancer Res.* **16**(9), 2605–2614 (2010).
98. S. Jiang et al., "Evaluation of breast tumor response to neoadjuvant chemotherapy with tomographic diffuse optical spectroscopy: case studies of tumor region-of-interest changes," *Radiology* **252**(2), 551–560 (2009).
99. L. C. Enfield et al., "Optical tomography of breast cancer-monitoring response to primary medical therapy," *Target Oncol.* **4**(3), 219–233 (2009).
100. Q. Zhu et al., "Noninvasive monitoring of breast cancer during neoadjuvant chemotherapy using optical tomography with ultrasound localization," *Neoplasia* **10**(10), 1028–1040 (2008).
101. R. Choe et al., "Diffuse optical tomography of breast cancer during neoadjuvant chemotherapy: a case study with comparison to MRI," *Med. Phys.* **32**(4), 1128–1139 (2005).
102. L. C. Enfield et al., "Monitoring the response to primary medical therapy for breast cancer using three- dimensional time-resolved optical mammography," *Technol. Cancer Res. Treat.* **10**(6), 533–547 (2011).

103. J. R. Weber et al., "Multispectral imaging of tissue absorption and scattering using spatial frequency domain imaging and a computed-tomography imaging spectrometer," *J. Biomed. Opt.* **16**(1), 011015 (2011).

104. D. Abookasis et al., "Imaging cortical absorption, scattering, and hemodynamic response during ischemic stroke using spatially modulated near-infrared illumination," *J. Biomed. Opt.* **14**(2), 024033 (2009).

105. D. J. Cuccia et al., "Quantitative in vivo imaging of tissue absorption, scattering, and hemoglobin concentration in rat cortex using spatially modulated structured light," in *In Vivo Optical Imaging of Brain Function*, R. D. Frostig, Ed., CRC Press, Boca Raton, Florida (2009).

106. A. Lin et al., "Spatial frequency domain imaging of intrinsic optical property contrast in a mouse model of Alzheimer's Disease," *Ann. Biomed. Eng.* **39**(4), 1349–1357 (2011).

107. S. Belanger et al., "Real-time diffuse optical tomography based on structured illumination," *J. Biomed. Opt.* **15**(1), 016006 (2010).

108. R. B. Saager et al., "Quantitative fluorescence imaging of protoporphyrin IX through determination of tissue optical properties in the spatial frequency domain," *J. Biomed. Opt.* **16**(12), 126013 (2011).

109. S. Gioux et al., "First-in-human pilot study of a spatial frequency domain oxygenation imaging system," *J. Biomed. Opt.* **16**(8), 086015 (2011).

110. M. Kaiser et al., "Noninvasive assessment of burn wound severity using optical technology: a review of current and future modalities," *Burns* **37**(3), 377–386 (2011).

111. A. Yafi et al., "Postoperative quantitative assessment of reconstructive tissue status in a cutaneous flap model using spatial frequency domain imaging," *Plast. Reconstr. Surg.* **127**(1), 117–130 (2011).

112. M. R. Pharaon et al., "Early detection of complete vascular occlusion in a pedicle flap model using quantitative [corrected] spectral imaging," *Plast. Reconstr. Surg.* **126**(6), 1924–1935 (2010).

113. R. B. Saager et al., "Method for depth-resolved quantitation of optical properties in layered media using spatially modulated quantitative spectroscopy," *J. Biomed. Opt.* **16**(7), 077002 (2011).

114. D. Yudovsky and A. J. Durkin, "Spatial frequency domain spectroscopy of two layer media," *J. Biomed. Opt.* **16**(10), 107005 (2011).

115. K. Licha, "Contrast agents for optical imaging," in *Topics in Current Chemistry*, Springer, Berlin (2002).

116. J. V. Frangioni, "New technologies for human cancer imaging," *J. Clin. Oncol.* **26**(24), 4012–4021 (2008).